

Can the Helium-detonation Model Explain the Observed Diversity of Type Ia Supernovae?

Wenxiong Li^{1,2}, Xiaofeng Wang^{1,3,4}, Mattia Bulla⁵, Yen-Chen Pan⁶, Lifan Wang⁷, Jun Mo¹, Jujia Zhang^{8,9}, Chengyuan Wu¹, Jicheng Zhang¹, Tianmeng Zhang^{1,1,1}, Danfeng Xiang¹, Han Lin¹, Hanna Sai¹, Xinghan Zhang¹, Zhihao Chen¹, and Shengyu Yan¹

¹ Physics Department and Tsinghua Center for Astrophysics (THCA), Tsinghua University, Beijing, 100084, People's Republic of China; li-wx15@tsinghua.org.cn, wang_xf@mail.tsinghua.edu.cn

The School of Physics and Astronomy, Tel Aviv University, Tel Aviv 69978, Israel
 Beijing Planetarium, Beijing Academy of Science and Technology, Beijing, 100089, People's Republic of China
 Purple Mountain Observatory, Chinese Academy of Sciences, Nanjing, 210023, People's Republic of China
 Nordita, KTH Royal Institute of Technology and Stockholm University, Roslagstullsbacken 23, SE-106 91 Stockholm, Sweden
 Graduate Institute of Astronomy, National Central University, 300 Jhongda Road, Zhongli, Taoyuan, 32001, Taiwan
 George P. and Cynthia Woods Mitchell Institute for Fundamental Physics & Astronomy, Texas A&M University, Department of Physics and Astronomy, 4242
 TAMU, College Station, TX 77843, USA

⁸ Yunnan Observatories (YNAO), Chinese Academy of Sciences (CAS), Kunming, 650216, People's Republic of China
⁹ Key Laboratory for the Structure and Evolution of Celestial Objects, CAS, Kunming, 650216, People's Republic of China
¹⁰ Key Laboratory of Optical Astronomy, National Astronomical Observatories, Chinese Academy of Sciences, 10101, Beijing, People's Republic of China
¹¹ School of Astronomy and Space Science, University of Chinese Academy of Sciences, 101408, Beijing, People's Republic of China
Received 2020 September 1; revised 2020 October 31; accepted 2020 November 10; published 2021 January 13

Abstract

We study a sample of 16 Type Ia supernovae (SNe Ia) having both spectroscopic and photometric observations within 2–3 days after the first light. The early B-V colors of such a sample tend to show a continuous distribution. For objects with normal ejecta velocity (NV), the C II λ 6580 feature is always visible in the early spectra, while it is absent or very weak in the high-velocity (HV) counterpart. Moreover, the velocities of the detached high-velocity features (HVFs) of the Ca II near-IR triplet (CaIR3) above the photosphere are found to be much higher in HV objects than in NV objects, with typical values exceeding 30,000 km s⁻¹ at 2–3 days. We further analyze the relation between the velocity shift of late-time [Fe II] lines ($\nu_{\rm [Fe II]}$) and host galaxy mass. We find that all HV objects have redshifted $\nu_{\rm [Fe II]}$, while NV objects have both blue- and redshifted $\nu_{\rm [Fe II]}$. It is interesting to point out that the objects with redshifted $\nu_{\rm [Fe II]}$ are all located in massive galaxies, implying that HV and a portion of NV objects may have similar progenitor metallicities and explosion mechanisms. We propose that, with a geometric/projected effect, the He-detonation model may account for the similarity in birthplace environment and the differences seen in some SNe Ia, including B-V colors, C II features, CaIR3 HVFs at early times, and $\nu_{\rm [Fe II]}$ in the nebular phase. Nevertheless, some features predicted by He-detonation simulation, such as the rapidly decreasing light curve, deviate from the observations, and some NV objects with blueshifted nebular $\nu_{\rm [Fe III]}$ may involve other explosion mechanisms.

Unified Astronomy Thesaurus concepts: Type Ia supernovae (1728); Observational astronomy (1145); Helium burning (716); Optical observation (1169)

1. Introduction

Type Ia supernovae (SNe Ia) are thought to be the thermonuclear runaway of a carbon–oxygen (C/O) white dwarf (WD) in a binary system. However, the physical properties of the companion star and the explosion mechanism of normal SNe Ia are still unclear (Howell 2011). One mechanism is the delayeddetonation (DDT) model: ignition of a Chandrasekhar-mass (M_{Ch}) WD, which requires expansion before the explosion (Nomoto et al. 1984; Khokhlov 1991). In this scenario, a WD accretes material from a nondegenerate companion star until it reaches $M_{\rm Ch}$ and explodes. Several three-dimensional simulations of near- M_{Ch} explosions have been published (Gamezo et al. 2005; Röpke & Niemeyer 2007; Bravo & García-Senz 2008; Seitenzahl et al. 2011; Röpke et al. 2012; Seitenzahl et al. 2013). Light curves and spectra of a normal SN Ia can be produced by this scenario (Seitenzahl et al. 2013; Sim et al. 2013). Blondin et al. (2015) suggested that the DDT model succeeds in reproducing observables of the high-velocity (HV) subgroup (see below). Another mechanism for normal SNe Ia is the violent merger of two WDs (Iben & Tutukov 1984; Webbink 1984).

Radiative transfer simulations for relatively massive WD pairs have shown a reasonable match with the spectra and light curves of normal SNe Ia (Pakmor et al. 2012; Moll et al. 2014). However, the strong polarization features arising from the significant asymmetries in this scenario are not observed in most SNe Ia (Bulla et al. 2016b).

Another explosion mechanism for SNe Ia is the sub- $M_{\rm Ch}$ Hedetonation (or double-detonation) model. There are two detonation processes in this model: the first one is the detonation of the accreted He on the surface of the progenitor, then the supersonic wave propagates on the surface, converges to the opposite side, and triggers the second one (Nomoto 1982a, 1982b; Livne 1990; Woosley & Weaver 1994; Hoeflich et al. 1996; Woosley & Kasen 2011). However, earlier-time models needed a thick He shell (\sim 0.1 M_{\odot}) and produced a Ti- and Ni-rich outer layer that is not observed in SNe Ia. Recent studies reveal that the minimal He-shell mass required to trigger a runaway explosion can be much lower than previous estimates (Shen & Moore 2014; Townsley et al. 2019), and the results of the simulations match the main

Table 1Sample of SNe Ia with Very Early-time Observations

Name	M_B (mag)	$\Delta m_{15}(B)$ (mag)	$v_{\rm Si,max} \ ({\rm km\ s}^{-1})$	References	Туре
SN 2002bo	-19.4 ± 0.4	1.13 ± 0.05	13000 ± 300	(1)	HV
SN 2009ig	-19.46 ± 0.08	0.90 ± 0.07	13500 ± 200	(2)	HV
SN 2011fe	-19.23 ± 0.09	1.07 ± 0.06	10500 ± 200	(3)	NV
SN 2012cg	-19.73 ± 0.02	0.86 ± 0.02	10500 ± 200	(4)	NV
SN 2012fr	-19.49 ± 0.06	0.85 ± 0.05	12120 ± 70	(5)	HV
iPTF 13ebh	-18.95 ± 0.07	1.76 ± 0.02	10400 ± 200	(6)	NV
SN 2013dy	-19.65 ± 0.40	0.90 ± 0.03	10200 ± 300	(7)	NV
SN 2013gy	-19.3 ± 0.2	1.23 ± 0.06	10180 ± 200	(8)	NV
iPTF 16abc	-19.56 ± 0.08	0.95 ± 0.01	10200 ± 300	(9)	NV
SN 2017cbv	-20.04 ± 0.09	1.06 ± 0.05	9600 ± 400	(10)	NV
SN 2017cfd	-19.3 ± 0.2	1.16 ± 0.11	11200 ± 200	(11)	NV
SN 2017erp	-19.1 ± 0.1	1.05 ± 0.06	10400 ± 200	(12)	NV
SN 2018gv	-19.0 ± 0.3	0.96 ± 0.04	11400 ± 200	(13)	NV
SN 2018yu	-19.5 ± 0.4	0.98 ± 0.01	10000 ± 300	(14)	NV
SN 2019ein	-18.81 ± 0.06	1.40 ± 0.01	13700 ± 300	(15)	HV
SN 2019np	-19.1 ± 0.3	0.95 ± 0.01	10000 ± 100	(16)	NV

References. (1) Benetti et al. (2004), Zheng et al. (2017); (2) Foley et al. (2012a), Marion et al. (2013), Stahl et al. (2020); (3) Nugent et al. (2011), Parrent et al. (2012); (4) Silverman et al. (2012), Marion et al. (2016), this work; (5) Childress et al. (2013), Zhang et al. (2014), Contreras et al. (2018); (6) Hsiao et al. (2015); (7) Zheng et al. (2013), Zhai et al. (2016); (8) Holmbo et al. (2019); (9) Miller et al. (2018); (10) Hosseinzadeh et al. (2017); (11) Han et al. (2020); (12) Brown et al. (2019); (13) Yang et al. (2020), this work; (14) this work; (15) Kawabata et al. (2020), Pellegrino et al. (2020), this work; (16) this work.

observable of SNe Ia (Kromer et al. 2010; Polin et al. 2019; Townsley et al. 2019).

Normal SNe Ia can be divided into two categories based on the Si II $\lambda 6355$ velocities at the maximum ($v_{\text{Si.max}}$): the HV $(v_{\rm Si,max}>11,800~{\rm km~s^{-1}})$ and normal-velocity (NV; $v_{\rm Si,max} \leq 11,800~{\rm km~s^{-1}})$ groups (Wang et al. 2009). Wang et al. (2009) further found that the HV group is redder and has a lower extinction ratio $R_V = A_V/(A_B - A_V)$, where A_X is the extinction in the X band. Wang et al. (2013) found that the $v_{Si,max}$ of SNe Ia show a bimodal distribution, where the HV group tends to be located in the inner regions of the host galaxies, while the NV group has wider distributions, suggesting different metallicity environments for these two groups. Pan et al. (2015) and Pan (2020) supported this idea by showing that HV objects tend to reside in massive galaxies with higher metallicity, while NV objects reside in both low-mass and massive host galaxies. Recently, Wang et al. (2019b) found that the HV group has excess blue flux during the early nebular phase, which may be caused by light scattering by the circumstellar material (CSM) around it, while the NV group does not have such features.

One promising way to study SNe Ia is to observe them as early as possible. Several scenarios only leave detectable imprints in the first few days after the onset of SN explosions. For instance, interaction between the SN ejecta and a nondegenerate companion may produce excess flux in the blue optical or ultraviolet (UV) bands (Kasen 2010). The very early observations of SN 2017cbv reveal a blue bump, which may favor a subgiant companion (Hosseinzadeh et al. 2017; but see Sand et al. 2018).

Thanks to the rapid developments of wide-field transient surveys, astronomers have discovered many more young SNe than in the past, which makes it possible to perform statistical researches of very young SNe Ia. Previous studies mainly focused on photometric properties (Jiang et al. 2018; Stritzinger et al. 2018; Bulla et al. 2020; Miller et al. 2020). Here we report the first statistical research that combines very early photometric and spectroscopic properties of normal SNe Ia. In

Section 2, we introduce our sample selection process and observations. In Section 3, we analyze several photometric and spectroscopic properties of our sample. In Section 4, we discuss the implications of our results for the explosion mechanism. The discussion and conclusions are presented in Section 5.

2. Sample Selection and Observations

We aim to select SNe Ia with good early multiband photometric and spectroscopic observations. Peculiar objects, i.e., super-Chandrasekhar SNe Ia, SNe Iax, are not included in our investigation due to possible different physical origins. We focus on SNe Ia with photometry and spectra from \sim 2 weeks before *B*-band maximum and at least four spectra before the maximum for each object. The sample contains 16 SNe, and the data mainly come from the literature. The basic information is listed in Table 1, including absolute *B*-band peak magnitude, $\Delta m_{15}(B)$, $v_{\rm Si,max}$, and subtype. Among the sample, SN 2017cfd has only two spectra. However, its first spectrum is early (at +3.5 days after the first light), and it has dense early photometry; thus, we include it for comparison.

Besides the data published in the literature, we have some new data for several objects: SNe 2019np, 2019ein (G. Xi et al. 2021, in preparation), 2018yu, 2018gv (W. Li et al. 2021, in preparation), and 2012cg. The broadband *BV*- and Sloan *gri*band images were obtained with the 0.8 m Tsinghua-NAOC Telescope in China (Huang et al. 2012) and processed using *Zrutyphot* (J. Mo et al. 2021, in preparation), including bias subtraction and flat-fielding. Template subtraction is performed when reducing these images. The *BV*- and *gri*-band photometry is calibrated into the Vega (Landolt 1992) and AB magnitude systems, respectively. The spectra were obtained with the Xinglong 2.16 m telescope (+BFOSC; Zhang et al. 2016), the Lijiang 2.4 m telescope (+YFOSC; Wang et al. 2019a), and the 3.5 m Astrophysics Research Consortium telescope. All spectra were reduced using standard IRAF routines.

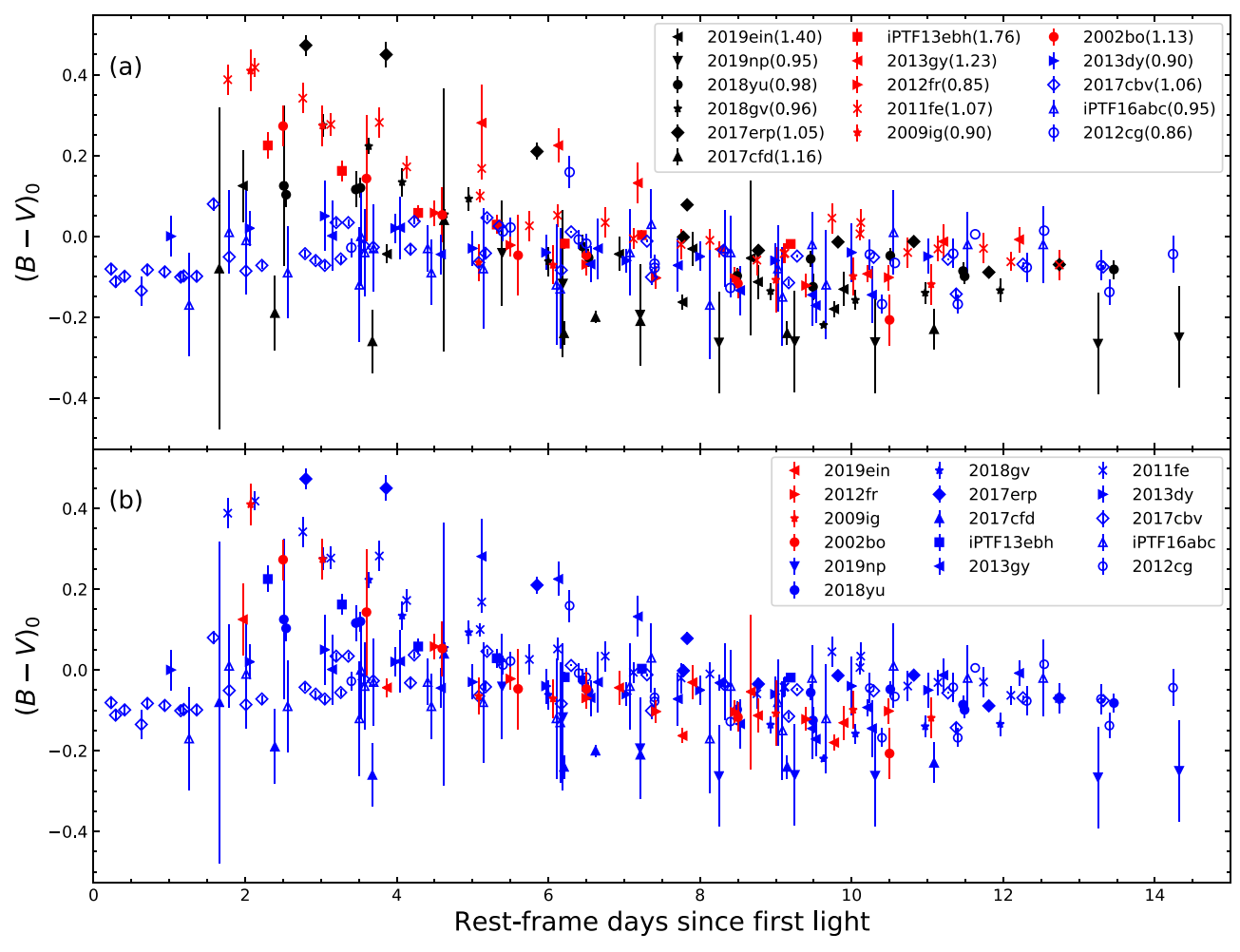


Figure 1. The $(B-V)_0$ color curves of our sample. All curves have been corrected for both reddening and time dilation. Each SN has the same symbol in each panel (but may have different colors). In the upper panel, the SNe included in Stritzinger et al. (2018) are marked in red or blue, while our new sample is in black. The $\Delta m_{15}(B)$ of each SN is given in parentheses. In the lower panel, the HV and NV groups are shown in red and blue, respectively. Open symbols represent three 91T/99aa-like SNe Ia.

3. Analysis

Here we investigate the photometric, spectroscopic, and host galaxy properties of our sample. Since the rise times of the light curves are different, we use the time relative to the first light as the time coordinate instead of the time relative to the *B*-band maximum, which is commonly used. The first-light time is different from the explosion time because there might be a dark phase that lasts for 1–2 days (Piro & Nakar 2013). We collect the first-light time of our sample from the literature while calculating the first-light time using Lmfit (Newville et al. 2016) for SN 2018yu and SN 2019np, yielding a rise time in the *V* band of 18.6 \pm 0.6 days for SN 2018yu and 19.7 \pm 0.6 days for SN 2019np. The multiband light curves of these two SNe are both well fit by a single power-law function.

3.1. Color Evolution

We display extinction-corrected $(B-V)_0$ color curves of our sample in Figure 1. For those SNe with known extinction, the values given in the literature are used. Otherwise, we fit the multiband light curves with SNooPy2 (Burns et al. 2011) to get

the host galaxy extinction in addition to the Galactic extinction (Schlafly & Finkbeiner 2011). Intrinsic colors from Burns et al. (2014) are used to infer the host extinction $E(B-V)_{\rm host}$, as well as $R_{\rm Vhost}$. The only object with both new and published photometry is SN 2019ein; our new results are consistent with the previous works (Kawabata et al. 2020; Pellegrino et al. 2020).

At 4 days after the first light, the $(B - V)_0$ color ranges from \sim -0.2 to 0.4 mag. This color dispersion gradually decreases to 0.3 mag several days later. Among our sample, SN 2017erp shows the reddest color in the early phase, i.e., $(B-V)_0 \sim$ 0.5 mag at $t \sim 2.8$ days, and it quickly evolves to ~ 0.05 mag at $t \sim 8$ days, indistinguishable from other objects. The object SN 2017cfd shows the bluest color, i.e., \sim -0.2 mag at $t \sim 2.5$ days, and the color mildly evolves after that. The distribution of $(B - V)_0$ seems to be continuous for our sample. Stritzinger et al. (2018) claimed that the early-time colors of SNe Ia tend to show evidence for two populations, i.e., red and blue. We overplot their sample together with our new sample in Figure 1(a). Among the new sample, SN 2018yu and SN 2019ein seem to be located between the red and blue groups, suggesting that the red and blue distinction is not sharp. It should be noted that the uncertainties are relatively large and fall within either the red or blue group for most of the data

¹² We notice that the first-light times from the literature are calculated with different fitting methods and may cause additional uncertainties.

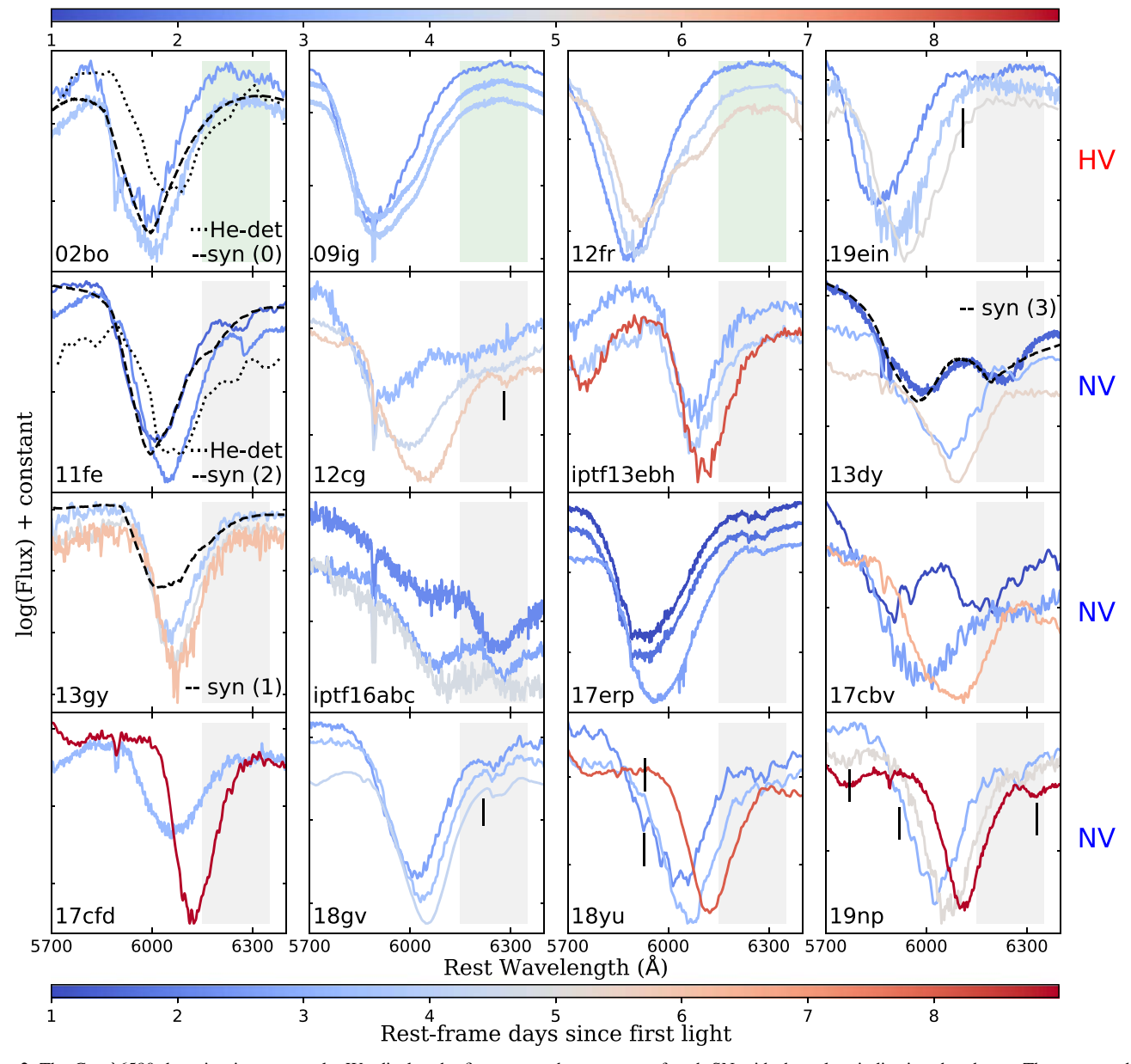


Figure 2. The C II λ 6580 detection in our sample. We display the first two or three spectra of each SN with the colors indicating the phases. The green and gray shaded areas show C II λ 6580 regions for carbon-negative and carbon-positive SNe, respectively. The SNe in the first row are HV objects, while the others are NV objects. We also plot the He-detonation (see Section 4) model spectra (black dotted lines) synthesized at t=+5 days from the explosion in the SN 2002bo (n_1 direction; see Figure 7) and SN 2011fe (n_3 direction) panels, as well as the SYNAPPS fit to the observed spectra of SNe 2002bo, 2011fe, 2013dy, and 2013gy at $t \sim +4$ days with the s_c value labeled in the legends (black dashed lines). New spectra are labeled by vertical black lines.

points in this sample. More early-time observations are needed to distinguish whether it is a continuous or bimodal distribution.

To examine the color evolution for different subtypes of SNe Ia, we marked the HV and NV groups with different colors, as shown in Figure 1(b). One can see that the HV objects initially have red colors and then evolve blueward with $(B-V)_0 \sim -0.1$ mag at $t \sim 5$ days. The distribution for the NV group is much wider in the early phase, ranging from -0.2 to +0.4 mag. The 91T/99aa-like objects are hot and luminous, with some common features, such as weak Si II features around the maximum and early excess flux (Jiang et al. 2018). In the $(B-V)_0$ color evolution diagram, these slow decliners tend to dominate the blue side at the early time.

3.2. Carbon Imprint

To investigate the unburned carbon in the ejecta, we examine the dominant C II absorption feature in optical spectra (i.e., C II λ 6580). This feature appears as a notch or plateau on the red edge of the Si II λ 6355 absorption feature. We display the C II λ 6580 region in the early spectra of all objects in Figure 2. Objects with (without) C II λ 6580 feature belong to the NV (HV) group, except for one HV object, SN 2019ein, which has a C II λ 6580 feature that quickly disappears within 3 days of the first light. This trend is consistent with Parrent et al. (2011). The mean $\Delta m_{15}(B)$ of objects with carbon features (carbon-positive objects) and without carbon features (carbon-negative objects) is 1.08 ± 0.03 and 1.06 ± 0.03 mag, respectively, suggesting that there is no trend between light-curve widths and C II features, as reported by Thomas et al. (2011) and Maguire et al. (2014).

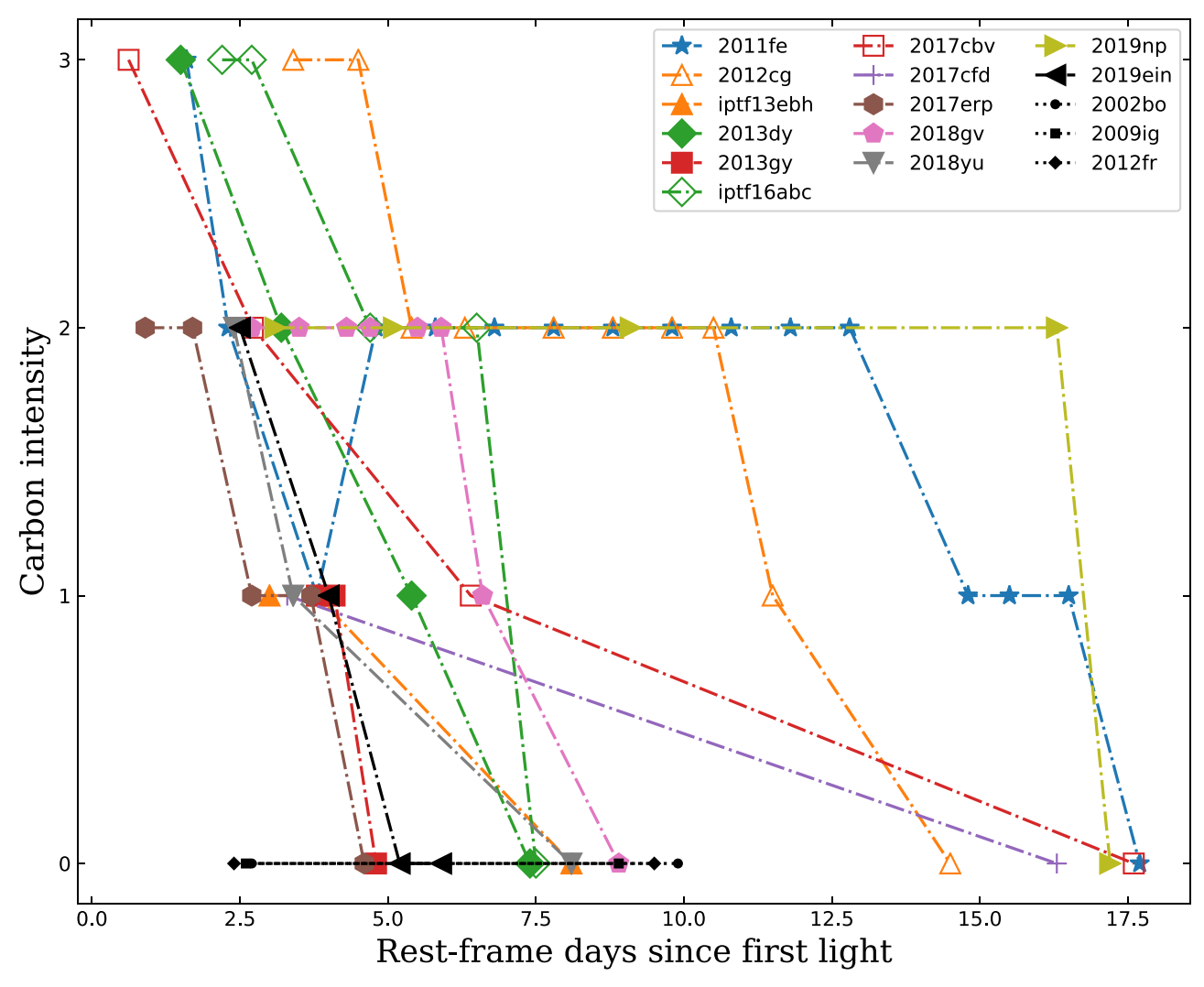


Figure 3. The C II λ 6580 intensity in the spectra, evaluated for our sample. The HV objects are marked by black symbols, while the NV objects are marked by colored filled symbols. The 91T/99aa-like objects are marked by open symbols.

The carbon-negative objects have $(B-V)_0 > 0.1$ mag at the very early phase and evolve rapidly blueward, consistent with one-dimensional He-detonation models with a thin helium shell (see Figure 6 of Polin et al. 2019), which have little unburned carbon left after the explosion (but see Section 4). Two NV objects, SN 2011fe and iPTF 13ebh, also have possible C I lines detected in their near-IR (NIR) spectra (Hsiao et al. 2013, 2015). However, Heringer et al. (2019) questioned the identification of these features because their simulations do not show significant neutral carbon.

As the C II λ 6580 features are usually weak and sometimes appear as a plateau, it is not easy to measure the pseudo-equivalent widths (pEWs). Therefore, we use a semiquantitative score (s_c) to describe their intensity. The scoring criteria and examples are as follows.

- 0: No C II $\lambda 6580$ feature, such as the first spectrum of SN 2002bo.
- 1: The feature appears as a plateau, such as the first spectrum of SN 2013gy.
- 2: The feature appears as a notch, such as the first spectrum of SN 2011fe.
- 3: The feature is strong enough to affect the profile of the Si II λ 6355 feature, such as the first spectrum of SN 2012cg.

We use the highly parameterized code SYNAPPS (Thomas et al. 2011) to identify the carbon absorption features. The difference between 0 and 1 is obtained by comparing the spectra with a carbon-free SYNAPPS fit; i.e., if the spectrum has no absorption feature but deviated from the fit, we score 1, otherwise we score 0. Other spectra are scored by eye inspection. Four representative SYNAPPS fits for $s_c = 0-3$ are overplotted in Figure 2. We plot the scores of all early spectra in Figure 3. This analysis confirms the trend mentioned above, namely, that HV objects have a quickly disappearing C II $\lambda 6580$ feature or no such feature at all, while NV objects generally have such a feature and last for a longer time. All three 91T/99aa-like objects also have a strong C II feature at early phase. We will discuss the implications of these results for the explosion mechanisms in Section 4.

3.3. Ca II NIR Triplet Features

We use multiple Gaussian profiles to fit the photospheric-velocity features (PVFs) and high-velocity features (HVFs) of the Ca II NIR triplet (CaIR3). The velocity and pEW of each absorption feature can be measured from the fit. Previous studies indicate that the HVFs of CaIR3 are common in the spectra of SNe Ia (Zhao et al. 2015). We plot the CaIR3 region

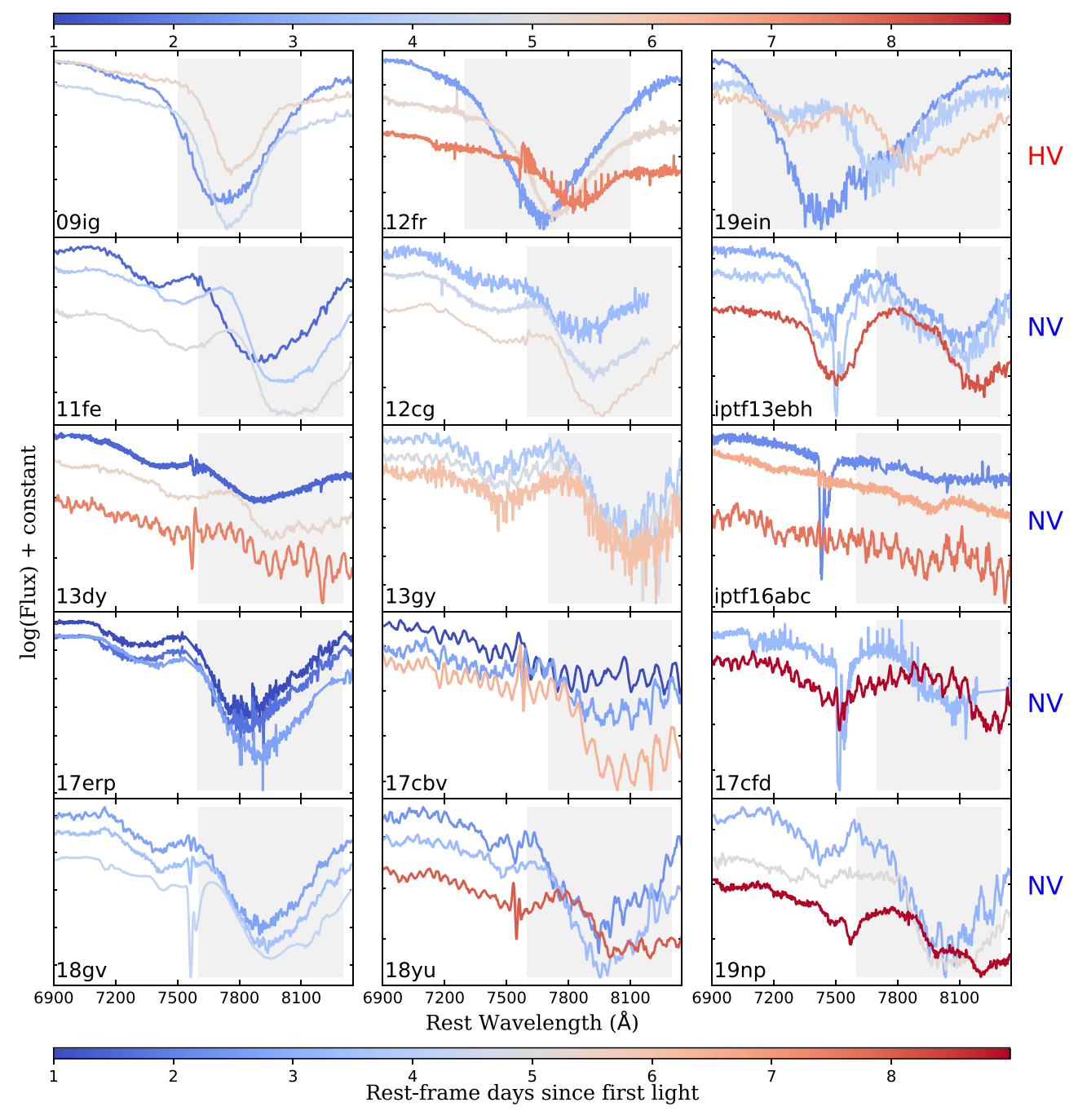


Figure 4. Similar to Figure 2. We display the CaIR3 region for the first two or three spectra of each SN, with the colors indicating the phases.

in the early spectra of our sample in Figure 4. In Figure 5, we investigate the velocity evolution of this spectral feature and find that all HV objects tend to have very high velocity, i.e., $>30,000 \, \mathrm{km \, s^{-1}}$, at $t \sim +3$ days. In comparison, the CaIR3 HVFs of all NV objects tend to have velocities below $30,000 \, \mathrm{km \, s^{-1}}$, except two luminous 99aa-like objects, iPTF 16abc and SN 2017cbv. Among the NV objects, SN 2017erp has the highest velocities with an early-time velocity of $\sim 29,000 \, \mathrm{km \, s^{-1}}$. The velocities of SN 2009ig and SN 2012fr are always above the NV groups, while the velocity of SN 2019ein declines rapidly and becomes lower than the NV groups. The median velocity of the CaIR3 HVFs of the HV group is $\sim 6000 \, \mathrm{km \, s^{-1}}$ higher than that of the NV group at the

early phase, and the difference gradually decreases to ${\sim}2000~\rm{km\,s}^{-1}$ at ${\sim}{+}14$ days after explosion.

3.4. Host Galaxy Mass

In order to constrain the physical origin of SNe Ia by combining early- and late-time observations and host galaxy properties, we study $\nu_{\rm Si,max}$; the velocity shift of late-time [Fe II] $\lambda7155$ features, $\nu_{\rm [Fe \ II]}$; and the host galaxy mass of the sample (see Figure 6). The spectral features from inner Fegroup regions dominate the late-time spectra, including [Fe II] $\lambda7155$, which is the strongest optical feature formed from the deflagration ashes. The SNe Ia with higher $\nu_{\rm Si,max}$ have more

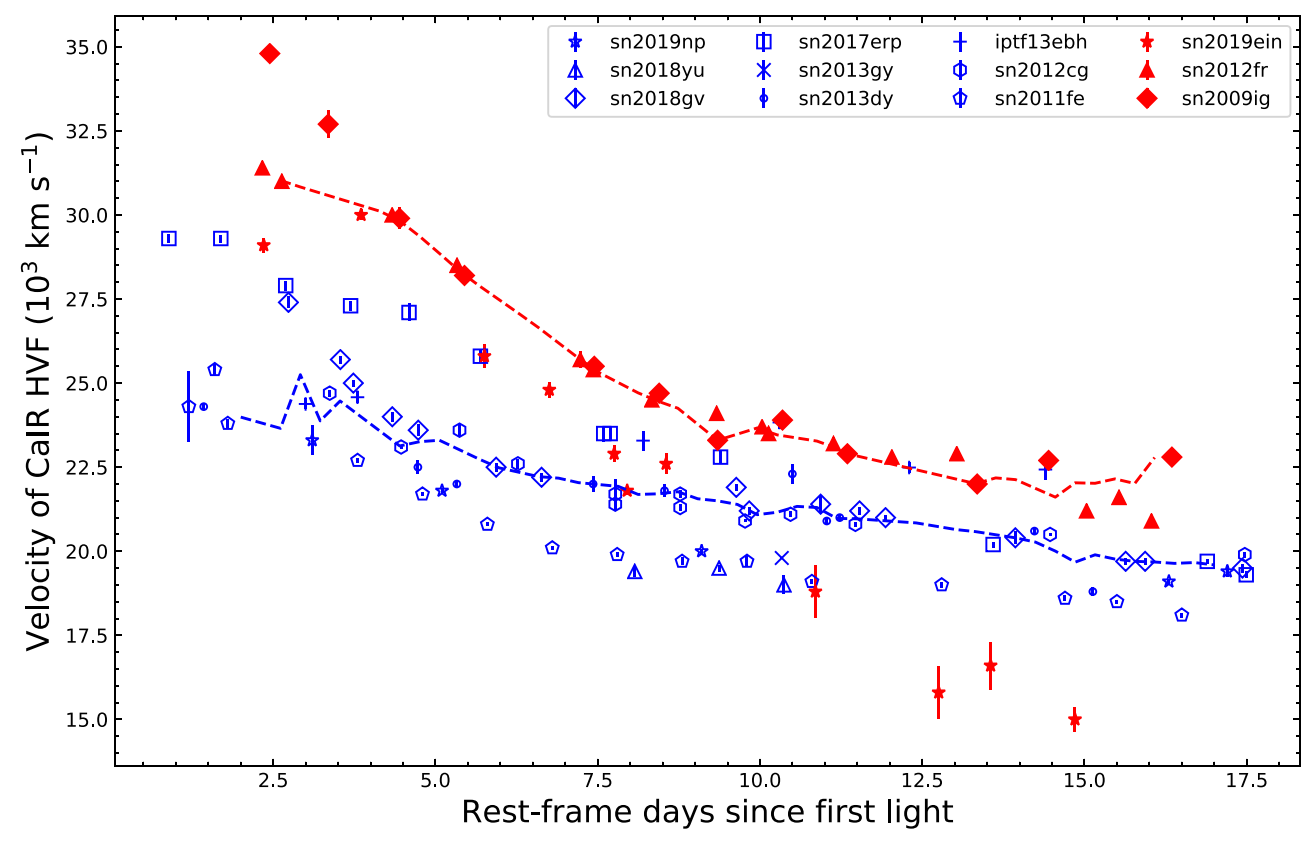


Figure 5. Velocity evolution of the CaIR3 triplet. The blue symbols represent the NV objects, while the red symbols represent the HV objects. The dashed lines are the median curves for the HV (red) and NV (blue) groups.

redshifted $v_{\rm [Fe~II]}$, implying asymmetric explosions for some SNe Ia (Maeda et al. 2010; Maguire et al. 2018). We add several SNe Ia with these parameters from the literature (Pan et al. 2015; Maguire et al. 2018; Rose et al. 2019; Pan 2020). We measure the $v_{\rm [Fe \ II]}$ of SNe 2017cbv and 2013gy using the Gaussian fit (see Section 3.3) and the host galaxy mass of SNe 2002dj, 2007le, 2010ev, 2013cs, 2013gy, and 2019ein using the same method adopted in Pan (2020). Pan et al. (2015) and Pan (2020) found that HV objects only occur in galaxies with $M_{\rm stellar} > 3 \times 10^9 \, (\sim 10^{9.5}) \, M_{\odot}$. Therefore, we choose the boundary between massive and low-mass galaxies as $\log(M_{\rm stellar}/M_{\odot}) = 9.5$. We notice that all HV objects have redshifted $v_{\rm [Fe \ II]}$, while NV objects have both redshifted and blueshifted $v_{\rm [Fe\ II]}$. Moreover, all objects with redshifted $v_{\rm [Fe\ II]}$ tend to reside in massive galaxies, while objects with blueshifted $v_{\rm [Fe\ II]}$ are located in both massive and low-mass galaxies. The $v_{\rm [Fe\ II]}$ seems to have a double-peak distribution (see the top panel of Figure 6), with one at $\sim -1000 \,\mathrm{km \, s^{-1}}$ and the other at $\sim +1500 \, \mathrm{km \, s^{-1}}$, which may indicate two populations. Nevertheless, the Si II velocity distribution measured around the maximum light does not reproduce the double Gaussian profile as reported by Wang et al. (2013), which means that our sample size is still too small. According to the mass-metallicity relation (Tremonti et al. 2004; Kewley & Ellison 2008), massive galaxies have, on average, higher metallicity than low-mass galaxies, suggesting that objects with redshifted $v_{\text{[Fe II]}}$ (including all HV objects) have metal-rich progenitor environments. We will discuss the implications of these phenomena in Section 4.

4. Discussion

4.1. Early-time (B - V)₀ Color Distribution

In this section, we further examine the differences and connections between NV and HV objects and provide implications for the explosion mechanism. Stritzinger et al. (2018) studied a sample of 13 SNe Ia, suggesting that they can be divided into red and blue groups according to the early B-V color, and the red group has a rapid evolution from red to blue. Jiang et al. (2018) reached a similar conclusion with 23 young SNe Ia. Han et al. (2020) also found that these two groups may exist by adding a sample of six more SNe, although we note that the distinction between these two subclasses is less significant when these events are added (see Figure 5 of Han et al. 2020). Our sample largely overlaps with the samples used in the above works, and the results inferred from the common sample are consistent. Bulla et al. (2020) studied the g - r (similar to B - V) curves of 65 SNe Ia from the Zwicky Transient Facility, discovered within 5 days of the first light, and found that the early colors were uniformly distributed and did not show any evidence for two separate groups. Our research adds a few new objects to this sample with early observations and also shows that the B-Vcolors do not have a distinct bimodal distribution either. One or more mechanisms, including companion interaction, ⁵⁶Ni distribution, and CSM interaction, can affect the early-time light and color curves. However, the quality of the current color curves is not high enough to distinguish different processes, and it is difficult to constrain the explosion mechanism from them.

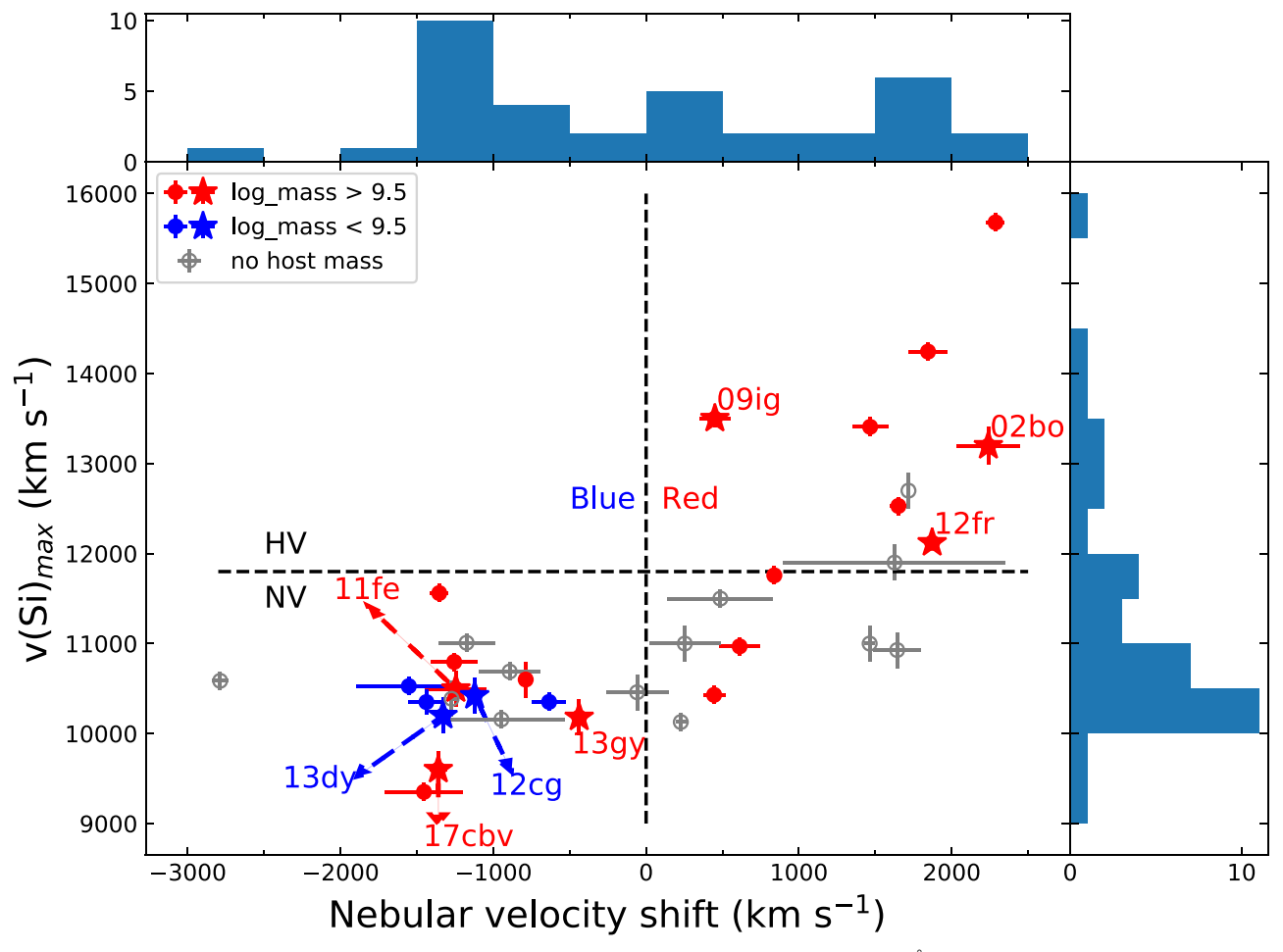


Figure 6. The Si II velocity measured from near-maximum-light spectra vs. the velocity shift of the [Fe II] 7155 Å feature inferred from the late-time spectra. The colors indicate the host galaxy masses (Pan et al. 2015; Maguire et al. 2018; Rose et al. 2019; Pan 2020). The SNe in our sample are marked by stars and labeled with their names. The horizontal and vertical dashed lines are the borders between the HV/NV group ($v_{\text{Si,max}} = 11,800 \text{ km s}^{-1}$) and the blue-/redshift of the nebular velocities ($v_{\text{[Fe II]}} = 0$), respectively. We also plot the histograms of $v_{\text{[Fe II]}}$ (top panel) and $v_{\text{Si,max}}$ (right panel).

4.2. The Link between the He-detonation Model and the Earlyphase Features

The absence or presence of a very weak carbon signal among the spectra of the HV group requires an explosion mechanism with high carbon-burning efficiency. The He-detonation scenario leaves almost no carbon after the explosion (Polin et al. 2019; Townsley et al. 2019). However, a small amount of carbon could leave weak orientation-dependent absorption features in the spectra, which are hardly observable at the north side 13 (n_1 - n_3 in Figure 7) but could be strongest at the south pole (n_5 in Figure 7). Therefore, a portion of NV objects with carbon absorption features could be observed from the south side of the He detonation, while HV objects could be observed from the north side. This is consistent with the viewing-angle effect of Si II velocity (around maximum) in the He-detonation model, where ejecta move at higher velocities in the northern hemisphere and lower velocities in the southern hemisphere (Bulla et al. 2016a; Townsley et al. 2019). In Figure 7, we show the spectral region around the Si II $\lambda 6355$ line predicted for the He-detonation "model 3m" presented by Kromer et al. (2010). This model is a modified version of "model 3" from Fink et al. (2010), where the helium shell is polluted by

34% of ¹²C to reduce the production of iron-group elements in the shell and thus provide a better match to the observed spectra of SNe Ia (see Kromer et al. 2010 for more details). Simulations have been carried out using the radiative transfer code ARTIS (Kromer & Sim 2009).

Spectra produced by our He-detonation model are shown in Figure 7 for five different viewing angles from north to south and at three different epochs: 5, 10, and 15 days after the explosion. Similar to the observations, the C II $\lambda 6580$ feature in the model spectra appears as a notch or plateau on the red edge of the Si II $\lambda 6355$ absorption feature. This carbon feature is absent for observers at the north pole and becomes stronger when moving toward the southern hemisphere, consistent with the idea that HV objects with little or no carbon could be Hedetonation explosions viewed from the ignition side, while a portion of NV objects are viewed from the opposite side. Figure 7 also shows how the presence of C II $\lambda 6580$ quickly weakens with time and disappears 15 days after the explosion (corresponding to \sim 2–5 days before peak going from south to north), even for an observer in the southern hemisphere. We plot the He-detonation spectra at 5 days from two directions, n_1 and n_3 , in the SN 2002bo and SN 2011fe panels of Figure 2. Despite the line profiles of Si II $\lambda 6355$ not entirely matching the observations, the nondetection of a C II feature in the spectrum of SN 2002bo is reproduced, while SN 2011fe does

 $[\]overline{^{13}}$ We regard the helium-detonation point (n_1 direction in Figure 7) as the north pole throughout the paper.

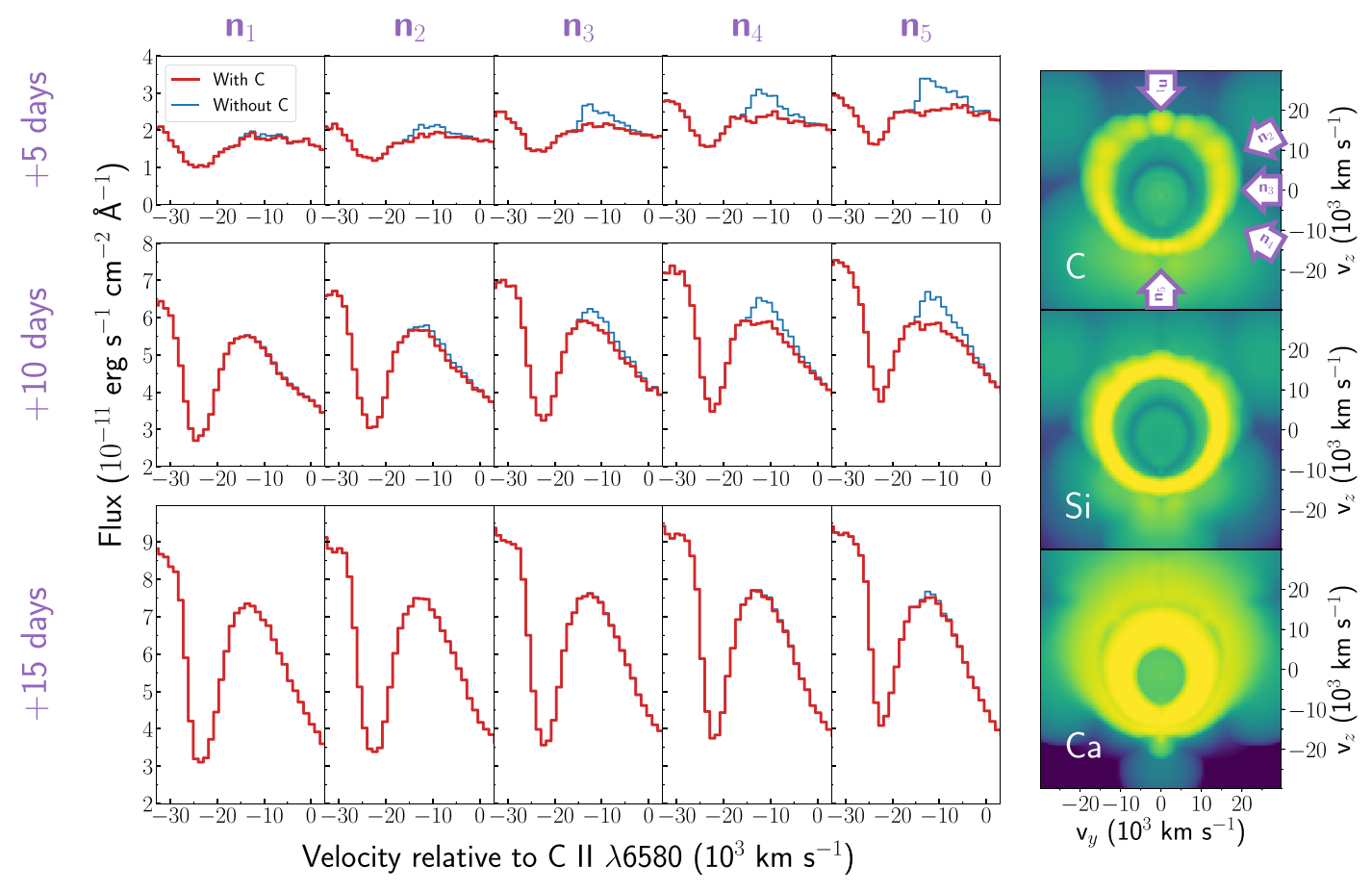


Figure 7. Carbon features predicted with ARTIS (Kromer & Sim 2009) for the double-detonation model 3m from Kromer et al. (2010). Left panels: wavelength region around the Si II λ 6355 and C II λ 6580 profiles at three different epochs (5, 10, and 15 days since explosion, from top to bottom) and for five different observers from north (left) to south (right). The predicted spectra are shown as a function of the C II λ 6580 velocity in red, while blue lines are spectra where carbon has been artificially removed. Therefore, the difference between the two spectra (red and blue lines) in each panel highlights the carbon contribution to the spectral region. Right panels: carbon (top), silicon (middle), and calcium (bottom) mass distribution in an inner slice of the model (yz-plane), with the five observer viewing angles n_1 – n_5 marked with arrows. The maps are shown 7.8 s after the explosion, when the ejecta are already in homologous expansion; i.e., densities drop with time as $\rho \propto t^{-3}$, but the C, Si, and Ca distributions are unchanged at the epochs investigated (+5, +10, and +15 days).

have such a feature in the early spectra. The DDT model is another candidate mechanism that leaves unburned carbon near the surface due to the deflagration process (Seitenzahl et al. 2013). Therefore, it cannot explain the absence of carbon in the outer ejecta of HV objects.

The HVFs have three proposed origins: density enhancement (DE), abundance enhancement (AE), and ionization effect (IE; Mazzali et al. 2005; Tanaka et al. 2008). The extremely high velocities of CaIR3 are ubiquitous among the early spectra of HV objects, implying that they may originate from the same mechanism. Synthesized Ca from He detonation at the north side can reach a velocity of more than 30,000 km s⁻¹, while the Ca at the south side has a much lower velocity (Figure 7). Townsley et al. (2019) also argue that the double-layer structure in the He-detonation model may produce AE in the outer ejecta and thus explain both the HVFs and PVFs of Si and Ca. Interaction between SN ejecta and CSM can produce DE or IE effects (Mulligan & Wheeler 2018; Mulligan et al. 2019), though it is difficult to consistently demonstrate the difference in HVFs of HV and NV SNe Ia. The DDT simulations that are most consistent with the observations of normal SNe Ia have multiple ignition sparks (N40 and N100 in Sim et al. 2013, which has 40 and 100 sparks, respectively); therefore, they are close to spherical symmetry. In principle, the

DDT model can result in HV ejecta (e.g., Khokhlov 1991). Although some three-dimensional simulations (e.g., the N1 and N3 models from Seitenzahl et al. 2013) can reproduce the HV intermediate-mass elements at the outermost layer of the SN ejecta, the ⁵⁶Ni yield seems to be higher than that observed for normal SNe Ia. Current DDT models seem to have difficulty producing the HVFs of some SNe Ia, especially those extreme HVFs seen in SN 2019ein (Pellegrino et al. 2020).

4.3. Bimodal Distribution of Si II and [Fe II] Velocities

The HV and NV groups were initially classified according to the $v_{\rm Si,max}$ (i.e., Wang et al. 2009). The observed $v_{\rm Si,max}$ distribution of SNe Ia tends to exhibit a double Gaussian distribution, while these two components have overlapping regions (see Figure 1 of Wang et al. 2013 and Figure 3 of Zhang et al. 2020). The HV profile is much broader, reaching a velocity as low as $<10,000\,{\rm km\,s^{-1}}$, while the HV tail of the NV profile extends a little into the HV region. If asymmetric He detonation is the explosion mechanism responsible for the HV SNe Ia, a portion of the NV objects may have the same explosion mechanism but with different viewing angles, which can explain the higher-velocity and broader Gaussian distribution. Objects like SN 2017erp with several characteristics of the HV group, such as red early-time color, a quickly

disappearing C II feature, and a relatively high velocity of CaIR3 HVFs, may have the same origin as the HV group, and their low $v_{Si,max}$ might result from the geometrical effect.

Maeda et al. (2010) and Maguire et al. (2018) found that SNe Ia with higher $v_{Si,max}$ tend to exhibit redshifted [Fe II] features in the nebular phase, implying an asymmetric explosion mechanism for some SNe Ia. Pan et al. (2015) and Pan (2020) found that HV objects tend to occur in massive host galaxies, while NV objects are located in both low-mass and massive host galaxies. Our finding that all HV objects have redshifted $v_{\rm [Fe \ II]}$ while the NV counterparts have both redshifted and blueshifted $v_{\rm [Fe \ II]}$ can fit into the sub- $M_{\rm ch}$ He-detonation models, where one would observe an HV object with redshifted Fe-group features when viewing from the He-detonation side (n_1 direction of Figure 7) and an NV object on the opposite side (south side) with blueshifted (or less redshifted) $v_{\text{[Fe II]}}$. The orientation-dependent Si-velocity trend is also in agreement with the synthetic spectra (see Figure 4 of Townsley et al. 2019). We also find that objects with redshifted $v_{\rm IFe~III}$, including all HV objects, are located in massive host galaxies ($\log(M_{\rm stellar}/M_{\odot}) > 9.5$), which implies that they have metal-rich progenitor environments. Metallicity plays an important role in the evolution of SNe Ia. Flörs et al. (2020) found that the sub- $M_{\rm ch}$ explosion simulations of $\sim Z_{\odot}$ progenitors can explain the Ni/Fe abundance measurements for the majority of normal SNe Ia, while only a small fraction (11%) of their sample is in agreement with $M_{\rm Ch}$ DDT explosion models. The sub- $M_{\rm ch}$ models include both He-detonation and violent merger scenarios. However, polarization measurements disfavor the strongly asymmetric violent merger scenario while supporting He-detonation and DDT models, which are more symmetric (Bulla et al. 2016a, 2016b). Therefore, we regard these results as support for the He-detonation scenario. Metalrich environments and progenitors are more likely to produce CSM around the progenitor systems, consistent with the observations that SNe Ia of the HV group are more likely to have abundant CSM than the NV group (Foley et al. 2012b; Wang et al. 2012, 2019b).

Polin et al. (2019) claimed that the explosions of WDs with different masses, rather than the different viewing angles, may cause the range of $v_{\rm Si,max}$. Pan et al. (2015) and Pan (2020) confirmed that the HV group tends to have metal-rich progenitors. At a given mass, stars with higher metallicities generally produce less massive WDs; thus, the HV group may originate from the sub- $M_{\rm Ch}$ progenitors. However, the one-dimensional models studied by Polin et al. (2019) cannot explain the asymmetries revealed from the nebular observations. The CaIR3 features of these models are also too weak to account for the observations.

4.4. Possible Progenitor Systems for He-detonation Scenario

To form a CO WD with a thin He shell, as required by the He-detonation model, we need the CO WD to accrete and accumulate helium from the companion star, either an He star or an He-rich WD (Liu et al. 2017; Wang et al. 2017; Wang 2018). One of the main differences between these two scenarios is the delay times—the time interval from the formation time of the primordial binaries to the SN explosion. The CO WD + He-star channel has shorter delay times; therefore, it should originate from younger populations (Wang et al. 2009). Wang et al. (2013) found that the HV objects, similar to SNe Ibc, are located in the inner and brighter regions

of host galaxies than the NV objects, which suggests a origin of younger progenitor populations. Pan (2020) found that the host galaxies of the HV group do not tend to be younger than the NV group by analyzing the global specific star formation of the host galaxies. However, the global properties may not reflect the local properties that were utilized by Wang et al. (2013). The first SN Ia with detection of the progenitor system in prediscovery images, SN 2012Z, is believed to have an He star as a companion star (McCully et al. 2014). The only He nova discovered so far, V445 Pup, is a WD with an $\sim M_{Ch}$ mass and can accumulate accreted He from its He-star companion after the outburst (Kato et al. 2008; Woudt et al. 2009). It should be noted that a WD with an $\sim M_{\rm Ch}$ mass may not produce normal SNe Ia through an He-detonation explosion because the central density is too large and produces too much ⁵⁶Ni (Fink et al. 2010). A system similar to V445 Pup but with a less massive CO WD could be a better candidate for an He-detonation explosion. Furthermore, the ejecta of the He nova outbursts may form circumstellar dust, which is more common around HV objects (Wang et al. 2019b). Förster et al. (2012) proposed that CSM around SNe Ia after the explosion is asymmetric, probably due to the asymmetric explosion mechanism. Combining the younger progenitor environments, prediscovery progenitor system detection, the possible progenitor candidate, and CSM around the progenitor system, we tend to favor a CO WD + He-star system for the progenitor system of the Hedetonation scenario, although the possibility of a CO WD + He-rich WD channel cannot be fully excluded.

5. Conclusion

We analyze a sample of 16 SNe Ia with early spectral and photometric observations, including four HV objects: SNe 2002bo, 2009ig, 2012fr, and 2019ein. We investigate the B-V color evolution of the sample and find that the color distribution tends to be continuous. The color dispersion is ~ 0.6 mag at t = 2-3 days since explosion and gradually decreases to ~ 0.3 mag at ~ 2 weeks after that. In the early spectra of SNe Ia, HV objects have no or only a weak C II $\lambda 6580$ feature, while this feature is prominent in NV objects. This contrast may be understood in terms of the He-detonation model, where the HV objects are observed from the heliumdetonation side, while the NV objects are observed from the opposite side. Moreover, the CaIR3 HVFs of HV objects are apparently higher than those of NV objects, exceeding 30,000 km s⁻¹ in the very early phase, and these HVFs can also be naturally explained by observing the SNe Ia toward the helium-detonation side. We analyze the relation between $v_{\text{Si,max}}$, $v_{\text{[Fe II]}}$, and the host galaxy mass. All HV objects have redshifted $v_{\rm [Fe~II]}$ and are located in massive galaxies, while NV objects have both blue- and redshifted $v_{\rm [Fe \ II]}$ and are located in both massive and low-mass galaxies. The SNe with redshifted $v_{\rm [Fe~II]}$ require an asymmetric explosion model, such as the Hedetonation model. The fact that all redshifted SNe are located in massive galaxies implies that they may have similar progenitor metallicities and explosion mechanisms.

We conclude that the He-detonation model can simultaneously explain several characteristics of HV SNe Ia and a portion of NV objects, and the observed differences between them may be caused by different observation orientations. The presence of two populations is also favored by the Si II velocity distribution. The current DDT models cannot explain the carbon signal and HVFs in the spectra. For the He-detonation

model, we propose that the CO WD + He-star progenitor system is more likely, though the CO WD + He-rich WD progenitor system cannot be fully excluded. However, some features predicted by He-detonation simulation deviate from the observations, such as the rapidly decreasing light curve (Shen et al. 2018; Townsley et al. 2019). Whether HV and NV objects are intrinsically different or HV and a portion of NV objects have a common origin but different viewing angles requires more evidence. Nevertheless, our work confirms that the HV group is a distinctive subgroup of SNe Ia. Future multidimensional and more realistic simulations may better match the observations. Larger samples of infancy SNe Ia, especially spectral observations, will provide more clues to the progenitor problem through color evolution, Fe-group element distribution, HVFs, etc. Combining early and nebular observations, as well as host galaxy properties, will help to better understand the physics underlying the observed subtypes of SNe Ia.

This work is supported by the National Natural Science Foundation of China (NSFC grants 11633002, 12033003, and 11761141001). The authors gratefully acknowledge the Gauss Centre for Supercomputing (GCS) for providing computing time through the John von Neumann Institute for Computing (NIC) on the GCS share of the supercomputer JUQUEEN (Stephan & Docter 2015) at Jülich Supercomputing Centre (JSC). The GCS is the alliance of the three national supercomputing centers HLRS (Universität Stuttgart), JSC (Forschungszentrum Jülich), and LRZ (Bayerische Akademie der Wissenschaften), funded by the German Federal Ministry of Education and Research (BMBF) and the German State Ministries for Research of Baden-Württemberg (MWK), Bayern (StMWFK), and Nordrhein-Westfalen (MIWF). J.Z. is supported by the National Natural Science Foundation of China (NSFC; grants 11773067 and 11403096), the Youth Innovation Promotion Association of the CAS (grant 2018081), and the Ten Thousand Talents Program of Yunnan for Top-notch Young Talents. L.W. is supported by NSF award AST-1817099.

We thank Y. Yang, S. Holmbo, P. Brown, W. Zheng, J. Vinkó, and K. Maguire for sharing the data used in this paper. We thank D. Townsley and J. Sun for helpful discussion on this paper.

Software: SWARP (Bertin et al. 2002), SExtractor (Bertin & Arnouts 1996), SCAMP (Bertin 2006), Matplotlib (Hunter 2007), NumPy (van der Walt et al. 2011), SciPy (Oliphant 2007), SNooPy2 (Burns et al. 2011), Lmfit (Newville et al. 2016), ARTIS (Kromer & Sim 2009; Bulla et al. 2015), and SYNAPPS (Thomas et al. 2011).

ORCID iDs

Wenxiong Li https://orcid.org/0000-0002-0096-3523
Xiaofeng Wang https://orcid.org/0000-0002-7334-2357
Mattia Bulla https://orcid.org/0000-0002-8255-5127
Jujia Zhang https://orcid.org/0000-0002-8296-2590
Chengyuan Wu https://orcid.org/0000-0002-2452-551X
Jicheng Zhang https://orcid.org/0000-0002-4052-9932
Tianmeng Zhang https://orcid.org/0000-0002-8531-5161
Danfeng Xiang https://orcid.org/0000-0002-1089-1519

References

Benetti, S., Meikle, P., Stehle, M., et al. 2004, MNRAS, 348, 261 Bertin, E. 2006, adass XV, 351, 112

```
Bertin, E., & Arnouts, S. 1996, A&A, 117, 393
Bertin, E., Mellier, Y., Radovich, M., et al. 2002, adass XI, 281, 228
Blondin, S., Dessart, L., & Hillier, D. J. 2015, MNRAS, 448, 2766
Bravo, E., & García-Senz, D. 2008, A&A, 478, 843
Brown, P. J., Hosseinzadeh, G., Jha, S. W., et al. 2019, ApJ, 877, 152
Bulla, M., Miller, A. A., Yao, Y., et al. 2020, ApJ, 902, 48
Bulla, M., Sim, S. A., & Kromer, M. 2015, MNRAS, 450, 967
Bulla, M., Sim, S. A., Kromer, M., et al. 2016a, MNRAS, 462, 1039
Bulla, M., Sim, S. A., Pakmor, R., et al. 2016b, MNRAS, 455, 1060
Burns, C. R., Stritzinger, M., Phillips, M. M., et al. 2011, AJ, 141, 19
Burns, C. R., Stritzinger, M., Phillips, M. M., et al. 2014, ApJ, 789, 32
Childress, M. J., Scalzo, R. A., Sim, S. A., et al. 2013, ApJ, 770, 29
Contreras, C., Phillips, M. M., Burns, C. R., et al. 2018, ApJ, 859, 24
Fink, M., Röpke, F. K., Hillebrandt, W., et al. 2010, A&A, 514, A53
Flörs, A., Spyromilio, J., Taubenberger, S., et al. 2020, MNRAS, 491, 2902
Foley, R. J., Challis, P. J., Filippenko, A. V., et al. 2012a, ApJ, 744, 38
Foley, R. J., Simon, J. D., Burns, C. R., et al. 2012b, ApJ, 752, 101
Förster, F., González-Gaitán, S., Anderson, J., et al. 2012, ApJL, 754, L21
Gamezo, V. N., Khokhlov, A. M., & Oran, E. S. 2005, ApJ, 623, 337
Han, X., Zheng, W., Stahl, B. E., et al. 2020, ApJ, 892, 142
Heringer, E., van Kerkwijk, M. H., Sim, S. A., et al. 2019, ApJ, 871, 250
Hoeflich, P., Khokhlov, A., Wheeler, J. C., et al. 1996, ApJL, 472, L81
Holmbo, S., Stritzinger, M. D., Shappee, B. J., et al. 2019, A&A, 627, A174
Hosseinzadeh, G., Sand, D. J., Valenti, S., et al. 2017, ApJL, 845, L11
Howell, D. A. 2011, NatCo. 2, 350
Hsiao, E. Y., Burns, C. R., Contreras, C., et al. 2015, A&A, 578, A9
Hsiao, E. Y., Marion, G. H., Phillips, M. M., et al. 2013, ApJ, 766, 72
Huang, F., Li, J.-Z., Wang, X.-F., et al. 2012, RAA, 12, 1585
Hunter, J. D. 2007, CSE, 9, 90
Iben, I., & Tutukov, A. V. 1984, ApJS, 54, 335
Jiang, J. an., Doi, M., Maeda, K., et al. 2018, ApJ, 865, 149
Kasen, D. 2010, ApJ, 708, 1025
Kato, M., Hachisu, I., Kiyota, S., et al. 2008, ApJ, 684, 1366
Kawabata, M., Maeda, K., Yamanaka, M., et al. 2020, ApJ, 893, 143
Kewley, L. J., & Ellison, S. L. 2008, ApJ, 681, 1183
Khokhlov, A. M. 1991, A&A, 245, 114
Kromer, M., & Sim, S. A. 2009, MNRAS, 398, 1809
Kromer, M., Sim, S. A., Fink, M., et al. 2010, ApJ, 719, 1067
Landolt, A. U. 1992, AJ, 104, 340
Liu, D., Wang, B., Wu, C., et al. 2017, A&A, 606, A136
Livne, E. 1990, ApJL, 354, L53
Maeda, K., Benetti, S., Stritzinger, M., et al. 2010, Natur, 466, 82
Maguire, K., Sim, S. A., Shingles, L., et al. 2018, MNRAS, 477, 3567
Maguire, K., Sullivan, M., Pan, Y.-C., et al. 2014, MNRAS, 444, 3258
Marion, G. H., Brown, P. J., Vinkó, J., et al. 2016, ApJ, 820, 92
Marion, G. H., Vinko, J., Wheeler, J. C., et al. 2013, ApJ, 777, 40
Mazzali, P. A., Benetti, S., Altavilla, G., et al. 2005, ApJL, 623, L37
McCully, C., Jha, S. W., Foley, R. J., et al. 2014, Natur, 512, 54
Miller, A. A., Cao, Y., Piro, A. L., et al. 2018, ApJ, 852, 100
Miller, A. A., Yao, Y., Bulla, M., et al. 2020, ApJ, 902, 47
Moll, R., Raskin, C., Kasen, D., et al. 2014, ApJ, 785, 105
Mulligan, B. W., & Wheeler, J. C. 2018, MNRAS, 476, 1299
Mulligan, B. W., Zhang, K., & Wheeler, J. C. 2019, MNRAS, 484, 4785
Newville, M., Stensitzki, T., Allen, D. B., et al. 2016, Lmfit: Non-Linear Least-
   Square Minimization and Curve-Fitting for Python, Astrophysics Source
   Code Library, ascl:1606.014
Nomoto, K. 1982a, ApJ, 253, 798
Nomoto, K. 1982b, ApJ, 257, 780
Nomoto, K., Thielemann, F.-K., & Yokoi, K. 1984, ApJ, 286, 644
Nugent, P. E., Sullivan, M., Cenko, S. B., et al. 2011, Natur, 480, 344
Oliphant, T. E. 2007, CSE, 9, 10
Pakmor, R., Kromer, M., Taubenberger, S., et al. 2012, ApJL, 747, L10
Pan, Y.-C. 2020, ApJL, 895, L5
Pan, Y.-C., Sullivan, M., Maguire, K., et al. 2015, MNRAS, 446, 354
Parrent, J. T., Howell, D. A., Friesen, B., et al. 2012, ApJL, 752, L26
Parrent, J. T., Thomas, R. C., Fesen, R. A., et al. 2011, ApJ, 732, 30
Pellegrino, C., Howell, D. A., Sarbadhicary, S. K., et al. 2020, ApJ, 897, 159
Piro, A. L., & Nakar, E. 2013, ApJ, 769, 67
Polin, A., Nugent, P., & Kasen, D. 2019, ApJ, 873, 84
Röpke, F. K., Kromer, M., Seitenzahl, I. R., et al. 2012, ApJL, 750, L19
Röpke, F. K., & Niemeyer, J. C. 2007, A&A, 464, 683
Rose, B. M., Garnavich, P. M., & Berg, M. A. 2019, ApJ, 874, 32
Sand, D. J., Graham, M. L., Botyánszki, J., et al. 2018, ApJ, 863, 24
Schlafly, E. F., & Finkbeiner, D. P. 2011, ApJ, 737, 103
Seitenzahl, I. R., Ciaraldi-Schoolmann, F., & Röpke, F. K. 2011, MNRAS,
```

414, 2709

```
Seitenzahl, I. R., Ciaraldi-Schoolmann, F., Röpke, F. K., et al. 2013, MNRAS,
  429, 1156
Shen, K. J., Kasen, D., Miles, B. J., et al. 2018, ApJ, 854, 52
Shen, K. J., & Moore, K. 2014, ApJ, 797, 46
Silverman, J. M., Ganeshalingam, M., Cenko, S. B., et al. 2012, ApJL, 756, L7
Sim, S. A., Seitenzahl, I. R., Kromer, M., et al. 2013, MNRAS, 436, 333
Stahl, B. E., Zheng, W., de Jaeger, T., et al. 2020, MNRAS, 492, 4325
Stephan, M., & Docter, J. 2015, JLSRF, 1, A1
Stritzinger, M. D., Shappee, B. J., Piro, A. L., et al. 2018, ApJL, 864, L35
Tanaka, M., Mazzali, P. A., Benetti, S., et al. 2008, ApJ, 677, 448
Thomas, R. C., Aldering, G., Antilogus, P., et al. 2011, ApJ, 743, 27
Thomas, R. C., Nugent, P. E., & Meza, J. C. 2011, PASP, 123, 237
Townsley, D. M., Miles, B. J., Shen, K. J., et al. 2019, ApJL, 878, L38
Tremonti, C. A., Heckman, T. M., Kauffmann, G., et al. 2004, ApJ, 613, 898
van der Walt, S., Colbert, S. C., & Varoquaux, G. 2011, CSE, 13, 22
Wang, B. 2018, RAA, 18, 049
Wang, B., Meng, X., Chen, X., et al. 2009, MNRAS, 395, 847
Wang, B., Podsiadlowski, P., & Han, Z. 2017, MNRAS, 472, 1593
```

```
Wang, C.-J., Bai, J.-M., Fan, Y.-F., et al. 2019a, RAA, 19, 149
Wang, X., Chen, J., Wang, L., et al. 2019b, ApJ, 882, 120
Wang, X., Filippenko, A. V., Ganeshalingam, M., et al. 2009, ApJL, 699,
Wang, X., Wang, L., Filippenko, A. V., et al. 2012, ApJ, 749, 126
Wang, X., Wang, L., Filippenko, A. V., et al. 2013, Sci, 340, 170
Webbink, R. F. 1984, ApJ, 277, 355
Woosley, S. E., & Kasen, D. 2011, ApJ, 734, 38
Woosley, S. E., & Weaver, T. A. 1994, ApJ, 423, 371
Woudt, P. A., Steeghs, D., Karovska, M., et al. 2009, ApJ, 706, 738
Yang, Y., Hoeflich, P., Baade, D., et al. 2020, ApJ, 902, 46
Zhai, Q., Zhang, J.-J., Wang, X.-F., et al. 2016, AJ, 151, 125
Zhang, J.-C., Fan, Z., Yan, J.-Z., et al. 2016, PASP, 128, 105004
Zhang, J.-J., Wang, X.-F., Bai, J.-M., et al. 2014, AJ, 148, 1
Zhang, K. D., Zheng, W., de Jaeger, T., et al. 2020, MNRAS, 499, 5325
Zhao, X., Wang, X., Maeda, K., et al. 2015, ApJS, 220, 20
Zheng, W., Kelly, P. L., & Filippenko, A. V. 2017, ApJ, 848, 66
Zheng, W., Silverman, J. M., Filippenko, A. V., et al. 2013, ApJL, 778, L15
```